International Journal of Nanomedicine

Dovepress
Taylor & Francis Group

Open Access Full Text Article

ORIGINAL RESEARCH

Effect of Photothermal Therapy Using Gold Nanoparticles Conjugated with Hyaluronic Acid in an Intracranial Murine Glioblastoma Model

Javier Domingo-Diez[1], Alice Foti[2], Óscar Casanova-Carvajal[1,3], Lorena Marrodán[1], Noelia Granado[4], Cristina Satriano[2], Ricardo Martínez-Murillo[4], José-Javier Serrano-Olmedo[1,5,6], Milagros Ramos-Gómez[1,5,6]

[1]Center for Biomedical Technology (CTB), Universidad Politécnica de Madrid (UPM), Madrid, 28223, Spain; [2]Nano Hybrid Biointerfaces Laboratory (NHBIL), Department of Chemical Sciences, University of Catania, Catania, 95125, Italy; [3]Departamento de Ingeniería Eléctrica, Electrónica, Automática y Física Aplicada, Escuela Técnica Superior de Ingeniería y Diseño Industrial ETSIDI, Universidad Politécnica de Madrid, Madrid, 28040, Spain; [4]Neurovascular Research Group, Department of Translational Neuroscience, Instituto Cajal, CSIC, Madrid, 28002, Spain; [5]Centro de Investigación Biomédica en Red para Bioingeniería, Biomateriales y Nanomedicina, Instituto de Salud Carlos III, Madrid, 28029, Spain; [6]Departamento de Tecnología Fotónica y Bioingeniería, ETSI Telecomunicaciones, Universidad Politécnica de Madrid, Madrid, 28040, Spain

Correspondence: Milagros Ramos-Gómez, Universidad Politécnica de Madrid (UPM), Madrid, 28223, Spain, Email milagros.ramos@ctb.upm.es

Purpose: Glioblastoma multiforme (GBM) is the most common and aggressive malignant brain tumor. Conventional treatments for GBM include surgery, chemotherapy, radiotherapy, or a combination of these. However, emerging therapies, such as hyperthermia treatments, are being developed. One of these new therapies is nanoparticle-mediated photothermal therapy (PTT), a non-invasive treatment that converts light into heat using photoagents such as plasmonic nanoparticles. High molecular weight hyaluronic acid (HA) has been described as a potential inhibitor of tumor progression and exhibits a high affinity for the CD44 receptor, which is present in GBM cells. The in vivo efficacy of gold nanorods (GNRs) biofunctionalized with HA-700kDa in PTT has been evaluated in a murine GBM model.

Animals and Methods: Adult male C57/BL-6 mice (N=15), 3–8-month-old, were used for PTT experiments. CT2A cells were injected into the mouse brain to establish a GBM model. Tumor-bearing mice were randomly divided into three groups: Control (untreated, n=5), GNRs (injected with GNRs, n=5) and PTT-treated (injected with GNRs and treated with laser, n=5). After GNR injection, mice were irradiated with a laser at 0.98 A (250mW) for 25 min over three consecutive days.

Results: As observed in the analysis of tumor sizes from all MR images, animals treated with a laser following GNR injection exhibited significantly smaller tumor sizes compared to control and GNR-treated animals one week after the treatment. In addition, PTT treatment led to a notable improvement in the exploratory behavior of the treated animals and an increase in their life expectancy compared to untreated control mice.

Conclusion: This study demonstrates the efficacy of GNR-based-PTT, applied to an orthotopic tumor model, using GNRs biofunctionalized with HA to target GBM CT2A cells. The treatment resulted in a reduction in tumor mass and an extension of life expectancy in GNR-PTT treated mice.

Keywords: Gold nanorods, photothermal therapy, glioblastoma, murine tumor model

Introduction

Glioblastoma multiforme (GBM) is the most common aggressive malignant primary brain tumor.[1] It is also defined by WHO grade IV wild-type astrocytic glioma.[2,3] GBM is mainly classified into primary GBM or isocitrate dehydrogenase (IDH) wild-type GBM, which may develop *de novo* and represents 90% of diagnoses, and secondary GBM or IDH mutant GBM, which results from the progression of a low-grade diffuse glioma (WHO grade II and III) and represents 10% of cases.[4] The incidence of GBM is 5 per 100,000 people in the 45–54 age group, and it increases with age and varies by sex, being 1.48 times more common in men.[1,5] In addition, GBM is more common in Caucasians than in other ethnic groups.[6]

Received: 22 April 2025
Accepted: 4 July 2025
Published: 25 July 2025

The development of neurological symptoms, such as neurological deficits, memory loss, personality changes, aphasia, or visual field defects, requires neurological evaluation over a period of weeks or months.[7] Magnetic resonance imaging is a widely used technique in clinical practice for diagnosis and follow-up.[5,6] Patients with GBM have a poor prognosis and overall survival from diagnosis is approximately 15 months, with only 5% surviving for 5 years.[8]

Conventional treatments for GBM include surgery, chemotherapy, and radiation, or a combination of these. Currently, the main strategy to treat GBM is surgery to remove the tumor mass, followed by chemotherapy with temozolomide and radiotherapy.[9–11] However, emerging therapies such as immunotherapy[12] or hyperthermia[13] are being developed to improve patient outcomes due to tumor resistance to chemotherapy and radiotherapy. In addition, new treatments can be used in combination with conventional therapies due to their synergistic effects.[14]

Nanoparticle-mediated photothermal therapy (PTT) is an emerging non-invasive treatment that converts light into heat using photoagents such as plasmonic nanoparticles (NPs). These NPs induce an increase in temperature to a hyperthermia range of 41–45°C in the target tissue, selectively eliminating cancer cells.[15] Heating of NPs is produced by an external light source, such as near infrared (NIR) laser.[16] PTT causes physiological changes in the tumor microenvironment, resulting in vasodilation and increased permeability of cancer cells. It also improves the efficacy of conventional therapies, including a reduction in the required dose of chemotherapy and radiotherapy.[17] Multiple studies have shown that PTT induces cell death through necrotic and apoptotic pathways, depending on the power of the NIR laser irradiation, the type of cancer cell, and the heat generated.[18–20] The impact of physiological changes on tumors caused by PTT can stimulate the immune system due to the release of exosomes and antigens from cancer cells, as well as an inflammatory response with upregulated expression of cytokines, all of which lead to the activation of immune cells.[21]

NPs are the agents in PTT that absorb light and convert it into heat. They must have good NIR absorption, biocompatibility and high photostability.[19] NPs for PTT typically consist of metal materials such as iron oxide, graphene or, most commonly, gold. They can be delivered specifically to the tumor area, avoiding cytotoxic effects on other healthy tissues. Finally, NPs can be activated by irradiation with a NIR laser only in the target tissue.[22] Different shapes of gold NPs such as nanospheres, nanocubes, nanoflowers and nanorods (GNRs), are useful in PTT and share several localized surface plasmon resonance (LSPR) properties.[23,24] These optical properties depend on the LSPR, a physical phenomenon in which electrons oscillate when exposed to light. In the case of GNRs, they exhibit two absorption bands: one weak in the visible region and another strong in the NIR.[25] This is advantageous compared to spherical gold NPs, which have a single absorption peak in the visible light region.[26–28] NPs tend to accumulate in tumor tissues due to the leaky vasculature and defective lymphatic vessels within the tumor (a well-known effect called the increased permeability and retention effect), along with a compromised blood-brain barrier in advanced GBM cases.[29]

To target NPs to cancer cells, various biomolecules that recognize cancer cells can be attached to their surface. This process, known as biofunctionalization, allows NPs to be specifically targeted to cancer cells. When GNRs are injected into the bloodstream, they are rapidly coated with non-specific serum proteins, forming a corona protein. This corona may change the properties and shape of the GNRs, allowing them to be recognized by the reticuloendothelial system (RES),[30] which would result in minimizing the PTT effect.[28] Spontaneous aggregation of GNRs may also reduce the PTT effect because the absorption range changes, making the NPs insensitive to the specific wavelength of the laser radiation used. Therefore, GNRs are typically coated with polyethylene glycol to avoid recognition by the RES and to prevent aggregation.

Several molecules present in GBM cells can serve as potential targets for ligands that can be used to biofunctionalize NPs for PTT.[31] Numerous studies have demonstrated the effectiveness of targeting molecules such as CD133[32] and nestin[33] to eliminate GBM cells. Another marker of interest is CD44, which is overexpressed in GBM cancer stem cells (GCSC). CD44 is a cell membrane glycoprotein primarily involved in cell adhesion and communication. It also plays a critical role in many biological processes, including angiogenesis, cytokine release, and leukocyte activation. In cancer, CD44 has multiple functions, including proliferation, migration, metastasis, invasion and epithelial-mesenchymal transition. Additionally, it also inhibits apoptosis and is associated with the development of resistance to chemotherapy and radiation.[26,34,35]

Hyaluronic acid (HA) is a natural mucopolysaccharide composed of D-glucuronic acid and N-acetyl-D-glucosamine, with different molecular weights (MW) ranging from a few thousand to 10 million Da. HA is the most abundant component in the extracellular matrix of adult soft tissues.[36] The main functions of HA are to maintain tissue hydration due to its negative charge and hydrophilic behavior, homeostasis, and resistance to mechanical forces. In addition, HA is

a strong ligand for CD44 receptors, which are involved in cell-cell and cell-matrix adhesion processes.[37] In pathological conditions, such as in GBM CT2A cells, cancer cells express characteristics and markers such as CD133 or Nanog, which are associated with GCSCs.[38] GCSCs express CD44 isoforms with enhanced HA binding capacity,[39,40] which affects signaling pathways involved in migration, metastasis, and invasion.[41] Depending on its molecular weight (MW), HA can exhibit different properties that either promote or inhibit cancer proliferation.[42] Low MW (<30 kDa) HA, a product of HA degradation by metalloproteases, is associated with increased tumor growth and invasion, thereby exacerbating the pathologic condition.[43] High MW (>500 kDa) HA inhibits the production of metalloproteases via the MAPK/Akt pathway and may inhibit tumor progression. Medium MW (50–350 kDa) and low MW HA promote cancer cell proliferation, cell adhesion, and metalloprotease expression.[44]

The interaction between CD44 and HA is of interest in nanomedicine for the synthesis of biofunctionalized NPs capable of targeting tumors, with many applications such as drug release by nanocarriers[45] or micelles.[46] However, not all roles of the CD44-HA interaction are well understood, so further investigation is needed. NP-based PTT is a promising candidate for cancer treatment and could be effective in combination with conventional therapies such as chemotherapy, radiotherapy, and immunotherapy. Previous studies with core-shell NPs of metallic gold and HA synthesized by a green one-pot approach[42] have demonstrated their versatility as anti-angiogenic platforms for tumor therapy applications.

The present study aims to determine the efficacy of GNRs biofunctionalized with HA of different MWs (GNRs-HA-200kDa and GNRs-HA-700kDa) in in vitro PTT using a murine GBM cell line. Given that high MW HA has been described as a potential inhibitor of tumor progression and that long chains of HA have high affinity for the CD44 receptor,[36] present in CT2A cells, the in vivo efficacy of GNRs-HA-700kDa in PTT was also evaluated in a murine GBM model.

Materials and Methods

Synthesis and Biofunctionalization of GNRs

Aqueous GNR dispersions were obtained by seed-mediated growth method.[25] For the preparation of seeds, 25 μL of 50 mM $HAuCl_4$ were added to 4.7 mL of 0.1 CTAB solution, in 29°C water-bath under gentle stirring. After 5 min, 300 μL of freshly prepared 10 mM $NaBH_4$ were added to the solution and stirred for 5 min, until color turned brown-yellow. As per the growth solution, 100 μL of 50 mM $HAuCl_4$ were added to 10 mL of 0.1 M CTAB solution under stirring for 10 min, in a 29°C water-bath, followed by the addition of 76 μL of 100 mM ascorbic acid (solution turned colorless) and 100 μL of 5 mM $AgNO_3$. Finally, 106 μL of seed solution were added and the solution left under vigorous stirring at 279°C for 15 min. Turn in color was observed at the end of this time. The as prepared GNR dispersion was purified by rinsing off the reactants' excess through two centrifugation steps (8000 × rpm, 30 min, 29°C), with water washing in between.

As per the synthesis of hybrid GNR-HA systems, a drop by drop addition of 0.2% w/v HA solution (two different molecular weights, 200 and 700 kDa) was used with a HA:GNR volume ratio of 1 to 10 of was of the purified nanorods (sample named 'pellet 2') to an aqueous solution of HA in a volume ratio of 1 to 10.

Physicochemical Characterization

The plasmonic features of GNR and GNR-HA systems were scrutinized by UV visible spectroscopy. The UV-visible spectra were collected by using quartz cuvettes with 1 and 0.1 cm optical path length on a Perkin Elmer UV-vis spectrometer (Lambda 2S, Waltham, MA, USA).

Cell Culture

CT2A glioma cells were purchased from Sigma-Aldrich (SCC194). Glioma cell line was maintained in DMEM (Gibco, USA) with phenol red supplemented with 10% heat inactivated fetal bovine serum (FBS), 2mM glutamine and 100 units/mL penicillin and 100 μg/mL streptomycin. CT2A cells were maintained in an incubator at 37 °C in a humidified atmosphere containing 5% CO_2 and 95% air. CT2A cells were passed twice a week to ensure their optimal growth. The CT2A cell line was used to perform the in vitro assays and to induce tumor growth in the mouse brain for the in vivo experiments.

Photothermal Device

An 808 nm-continuous wave laser (Fiber Coupled Laser System, HJ Optronics, Inc., San Jose, CA, USA) was used for irradiation. It has a maximum power of 5W connected to a collimator lens (F-C5S3-780, Newport Corporation, Irvine, CA, USA) through a one-meter-long multimode optical fiber with a core diameter of 600μm and a power transmission efficiency of 90%-99% (Changchun New Industries, China). In the in vitro experiments, the 96-multiwell plates were irradiated from the bottom through the fixed collimator. For the in vivo studies, mice were irradiated from the top once the collimator was fixed vertically to the stereotaxic apparatus (David Kopf Instruments, Tujunga, CA, USA). To adjust the irradiation power accurately, the optic fiber was connected to a power meter (PM USB LM-10, Coherent Inc, Santa Clara, CA, USA) by an SMA fiber adapter (PN 1098589, Coherent Inc, Santa Clara, CA, USA), and the software PowerMaxPC (Coherent Inc, Santa Clara, CA, USA) was used to operate it.

In vitro PTT Experiments

CT2A cells were seeded at a density of 7×10^3 cells/well in a 96-multiwell plate. After 24h of incubation with HA-GNRs (1:100 dilution). CT2A cells were irradiated at 4,5W for 10 min.[18] *For* in vitro PTT treatments, DMEM supplemented with 10% FBS was replaced with phenol red-free DMEM without FBS. Cell viability assays were performed to assess the effectiveness of the in vitro PTT experiments.

Cell Viability Assays

Two methods were employed for assessing the cell viability after HA-GNRs incubation and in vitro PTT treatments: the XTT assay and Calcein/propidium iodide (PI) staining.

The XTT assay was performed using the XTT kit (AppliChem), where the reduction of 2,3-bis-(2-methoxy-4-nitro-5-sulfophenyl)-2H-tetrazolium-5-carboxanilide salt (XTT) to a water-soluble dye occurs only in viable cells due to specific enzymes.[47] The absorbance of each well was measured spectrophotometrically at 450 nm using an ELX808 microplate reader (BioTeK, Winooski, VT, USA). For the calcein/PI dual-staining assay, a final concentration of 1 μM calcein (Invitrogen, Molecular Probes) and 2 μM PI (Sigma-Aldrich) was used to stain living cells in green and dead cells in red, respectively. These markers were added to each well, and fluorescence was evaluated with using an inverted Leica DMI300 microscope equipped with a Leica DC100 digital camera (Leica, Nussloch, Germany) after incubating the cells for 20 min at 37 °C in the dark.

Mouse Brain Tumor Model

The CT2A cell line is highly tumorigenic, with a successful rate to develop intracranial tumors that result in high mortality within 3 to 8 weeks post-injection. Tumors formed by CT2A cells exhibit noncohesive, diffuse, infiltrative, highly proliferative, and hemorrhagic features, resembling those of human GBM.[38,48] All experimental procedures involving animals were carried out in accordance with Spanish regulations for animal care (Laws 53/2013 and ECC/566/2015). The procedures were approved by the Ethics Committee of the Universidad Politécnica de Madrid and the Regional Government of Madrid (authorization code: PROEX 187.3/24) and were conducted in compliance with the Animal Research Reporting of In Vivo Experiments (ARRIVE) guidelines. C57/BL-6 adult male mice, 3–8 month old, were housed in an animal room with a 12:12 light:dark cycle, controlled temperature and with free access to food and water. CT2A tumor model was developed in mice as described previously by Martínez-Murillo.[49] Briefly, CT2A cancer cells ($8x10^4$ cells/4 μL in PBS) were stereotactically injected into the mouse brain under isoflurane anesthesia (Nuzoa, Madrid, Spain), using a Hamilton syringe (Hamilton, Reno, NV, USA) and a mouse stereotaxic frame (David Kopf Instruments, Tujunga, CA, USA). The cells were implanted at the following coordinates relative to bregma: - 6 mm lateral −2.25mm antero-posterior, and 3 mm in depth.

In vivo PTT Experiments

Mice were randomly divided into three groups: control (untreated tumor, n=5), GNRs (tumor + GNR injection, n=5) and PTT treated (tumor + GNR injection followed by laser application, n=5), with a total sample size of N=15 animals. The

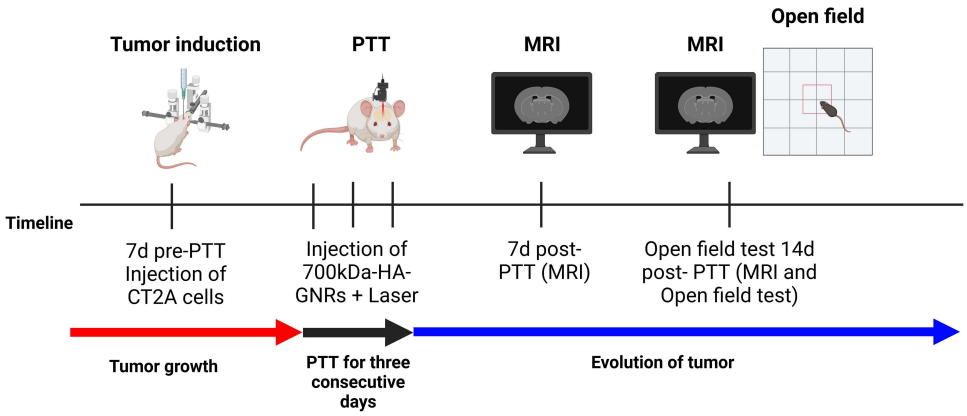

Figure 1 Timeline of the experimental design for PTT experiments on C57BL6 mice.

absence of any effect of laser irradiation on tumor size was previously determined.[32] Four microliters of the high MW GNRs (700-kDa-HA-GNRs) diluted 1:100 were gradually injected at a rate of 1µL per minute in the GNRs and PTT treated groups. After GNR injection, mice were irradiated with a laser at 0.98 A (250mW) for 25 min over three consecutive days, with the laser positioned on the hole of the skull where the cells and the GNRs were previously injected, as illustrated in Figure 1. During the surgical procedures, an electrical blanket was used to control the mouse temperature.

Magnetic Resonance Imaging (MRI) Acquisition

MRI scans were performed using a BIOSPEC BMT 47/40 (Bruker, Ettlingen, Germany) operating at 4.7 Teslas and equipped with a 12 cm actively shielded gradient system. Scan were performed at 7 and 15 days after laser irradiation to assess the size, location, and evolution of the tumor. Mice were anesthetized with pentobarbital (10 mg/kg) and atropine (90 mg/kg). Once fully sedated, the contrast agent gadopentetate dimeglumine (0.4 mmol/kg, Gadolinium, Magnevist, Schering, Germany) was injected. In order to avoid unexpected movements, the mice were positioned prone inside a cradle. A respiration sensor was used during MRI scans to monitor the vital functions of the mice. Firstly, T2 weighted images were acquired using a fast spin echo sequence with the following parameters: TR= 4000 ms, effective TE= 60 ms, FOV= 3 cm, slice thickness=1 mm and matrix= 256×192. This matrix was increased to obtain images with a size of 256×256 pixels. After that, T1-images were acquired using the same parameters described above. Tumor volume was determined using ParaVision software (Bruker, Ettlingen, Germany).

Behavioral Test

Mice were subjected to the open field test to evaluate their exploratory capacity. They were placed in an opaque box (40x30x30cm) without a lid for 5 minutes. The movement of each animal was continuously recorded to analyze the distance traveled and the velocity. Additionally, heatmaps and trajectories of the animals were visually analyzed using Ethovision XT© software.

Immunohistochemistry

At the end of the experiment, the animals were anesthetized with an overdose of xylazine/ketamine and intracardially perfused with freshly prepared, 4% paraformaldehyde (in 0.1 M phosphate buffer, pH 7.4). Brains were removed, postfixed for 12 h in the same fixative at 4 °C, and subsequently dehydrated in 30% sucrose solution at 4 °C until sunk. Coronal sections, 35 µm thick, were collected using a freezing microtome (Leica CM1950). Serial sections were used for immunohistochemistry using the following antibodies: nestin 1:200 (Merck), Iba1 1:1000 (Abcam) and Activated Caspase 3 1:800 (Invitrogen). After that, sections were incubated with the following secondary antibodies anti-rabbit Cy3, anti-mouse-FITC, diluted 1:200 (Invitrogen, Molecular Probes, USA) for 2h at room temperature in the dark. In

https://doi.org/10.2147/IJN.S525462

addition, nuclei were stained with Hoechst at 1:1000 in PBS for 30 minutes. Images were taken with an inverted Leica DMI300 microscope equipped with a Leica DC100 digital camera (Leica, Nussloch, Germany).

Statistical Analysis

The results are presented as the mean ± standard error of the mean from three to four experiments, unless otherwise specified. Statistical analyses were performed using GraphPad Prism software (San Diego, CA, USA). Normality was assessed with the Shapiro-Wilk test. Data were then analyzed using one-way analysis of variance (ANOVA) followed by Tukey's honestly significant difference post hoc test for parametric data, or the Kruskal–Wallis test for non-parametric data. A significance level of $P<0.05$ was selected. Survival analyses were conducted using the Kaplan-Meier test to assess the efficacy of PTT treatments in the in vivo experiments.

Results

Characterization of GNRs

UV-visible spectra of GNRs before and after purification by two steps of centrifugation are shown in Figure 2. As expected, both the as prepared and the purified GNRs exhibit the typical plasmonic bands of asymmetrical rod-shaped nanoparticles. Specifically, in Figures 2 and 3 two absorption bands are clearly visible, namely a band with higher absorbance in the near-infrared (NIR) region (~ 800 nm, longitudinal band, λ_L), and band lower in absorbance falling in the visible region (~ 512 nm), generated by electron oscillation along the transverse axis (λ_T). The transverse plasmonic band is centered at a wavelength value comparable to that of spherical gold nanoparticles of about 10 nm in size.[28]

Figure 3 shows the spectra of the GNR hybrid systems with HA200 (Figure 3A) and HA700 (Figure 3B), and points to a significant interaction among the metal nanoparticles and the polymer chains, as evidenced by a red-shift of λ_L for both GNRs, GNR/HA200 and GNR/HA700. The quantitative analysis of the optical parameters for the spectra reported in Figures 2 and 3 are given in Table 1, in terms of λ_T, λ_L and the respective values of absorbance. According to the following equations (1–2):[50]

$$\varepsilon = 0.01203\lambda_L - 4.79151 \quad (1)$$

$$\lambda_L = (53.71R - 42.29)\varepsilon + 495.14 \quad (2)$$

The aspect ratio (R) and the nanoparticle concentration (C, in nmol/L) can be calculated.

It should be noted that, after the purification (performed by two steps of centrifugation at 8,000 r.p.m, 30 min, with MilliQ water washing in between), the CTAB-capped GNRs exhibit a decreased ratio, namely from R=4.4 to R=4.1. This

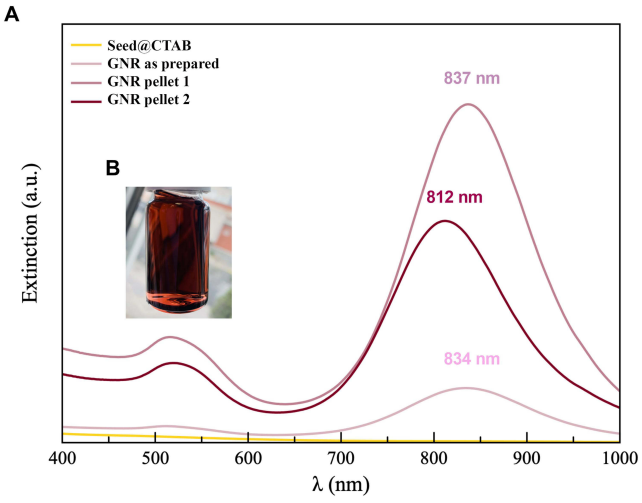

Figure 2 UV-visible spectra (optical path b=0.1 cm) of GNR (**A**) before (10x dilution of the as prepared nanorods) and after purification (10x dilution of the pellet samples). Image of a vial containing as prepared GNRs (**B**).

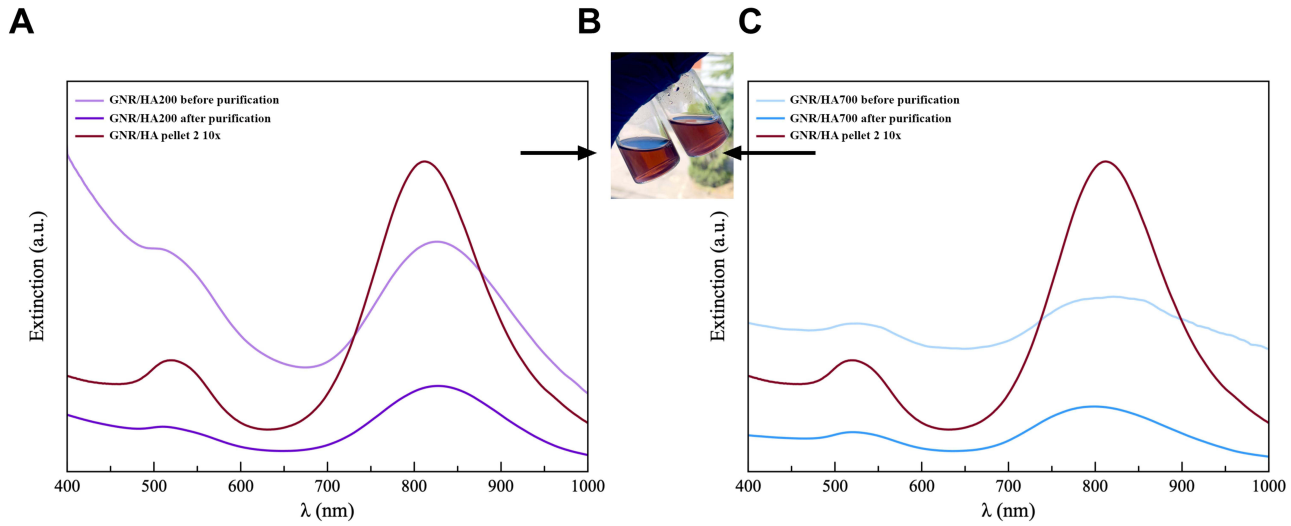

Figure 3 UV-visible spectra (optical path b=1) of GNR-HA hybrids prepared by using hyaluronan at 200 kDa MW (HA200, (**A**) or hyaluronan at 700 kDa MW (HA700, **C**). Image of vials containing GNR-HA (**B**).

fact is likely due to the partial removal of CTAB shell around the nanoparticles and the consequent partial aggregation effect.

Concerning the hybrid GNR samples, GNR/HA200 and GNR/HA700, before the purification, the nanoparticles exhibit, together with the red shift on the λ_L, an increased aspect ratio. This finding suggests a preferential interaction of the hyaluronan chains with the most 'defective' surface of the rod's basal planes instead of the lateral surface of the cylinders.

Also, for the hybrid GNR samples, GNR/HA200 and GNR/HA700, we attempted the purification. However, in this case, already after one step of centrifugation (15 min at 10,000 r.p.m), a massive aggregation was observed, and the nanoparticles precipitated onto the walls of the Eppendorf tubes (see Figure 4).

Accordingly, we recovered the supernatant (sample named "GNR/HA" after purification) and the spectra indicated a decrease of approximately 62% in the nanoparticle concentration.

Instead of having a hybrid GNR/HA system where the polymer chains "decorate" the nanoparticle surface, a polymer matrix embeds the nanorods. As support of this hypothesis, we can observe from Table 1 that the decrease in the nanoparticle concentration was more evident for HA700 than for HA200.

Table 1 SPR Values of wavelength and absorbance at the maximum of the transversal (λ_T, A_T) and longitudinal (λ_L, A_L) plasmon band, the calculated Aspect Ratio (R) for GNR, GNR/HA200, and GNR/HA700. The Last Column Reports the Calculated Concentration (C) for the Not Diluted Samples.

Sample	λ_T (nm)	A_T	λ_L (nm)	A_L	R	C (nM)
GNR as prepared (10x dil.)	512	0.12	834	0.39	4.4	0.7
GNR pellet 1 (10x dil.)	516	7.6	837	2.43	4.4	4.6
GNR pellet 2 (10x dil.)	516	5.7	812	1.59	4.1	3.2
GNR/HA200 before purification	512	1.14	827	1.18	4.3	0.2
GNR/HA200 after purification	512	0.23	827	0.44	4.3	0.08
GNR/HA700 before purification	521	0.76	822	0.9	4.2	0.2
GNR/HA700 after purification	521	0.2	800	0.33	4.0	0.07

https://doi.org/10.2147/IJN.S525462

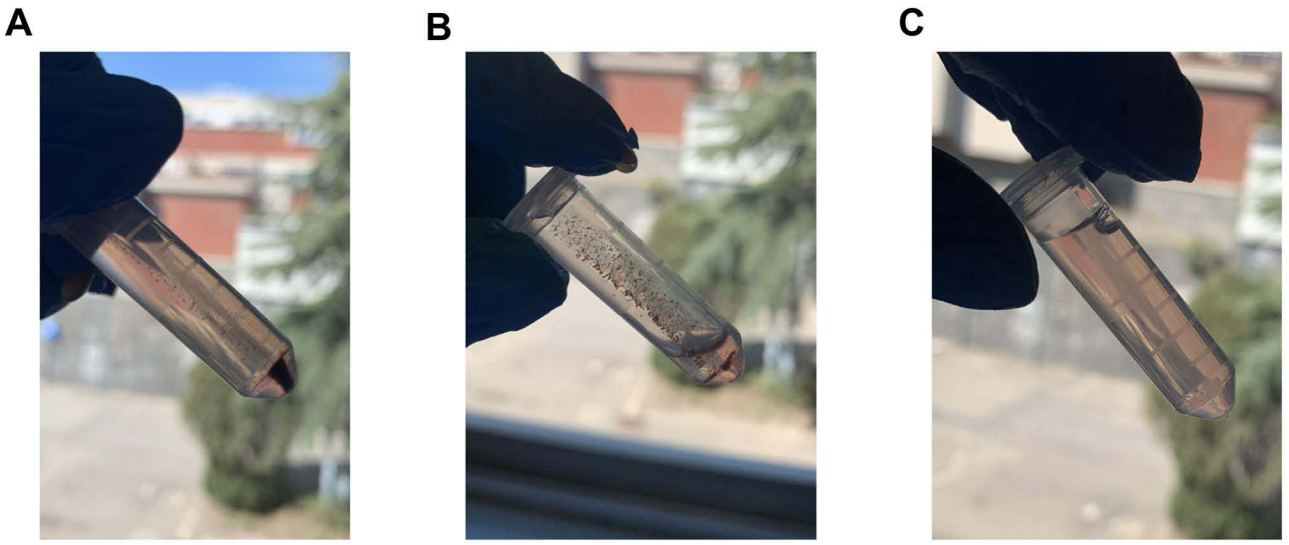

Figure 4 Representative photographs of the GNR/HA samples after the purification procedure. From left to right: immediately after the centrifugation (**A**), the aggregates residues on the Eppendorf (**B**), and the supernatant (**C**) (sample named "GNR/HA after purification").

In vitro PTT Experiments

Previous to determine the effectiveness of in vitro PTT, the cytocompatibility of the HA-GNRs employed in this study was assessed. To determine the impact of GNR concentration on cell viability, both sizes of HA-GNRs (200 and 700 kDa) were incubated at increasing concentrations with CT2A cells for 24 hours. Cell viability was then determined by means of XTT (Figure 5A) and Calcein/PI assays (Figures 5C). The results showed that cell viability was not compromised at a 1:100 dilution with both types of GNRs, 200 and 700 kDa HA-GNRs. The cytotoxicity profiles of both types of GNRs were very similar, consistent with the fact that their synthesis and subsequent HA biofunctionalization followed the same process, with the only difference being the molecular weight of the HA molecule attached to the GNRs. Based on these results, a 1:100 dilution was selected as the optimal GNR concentration for conducting PTT

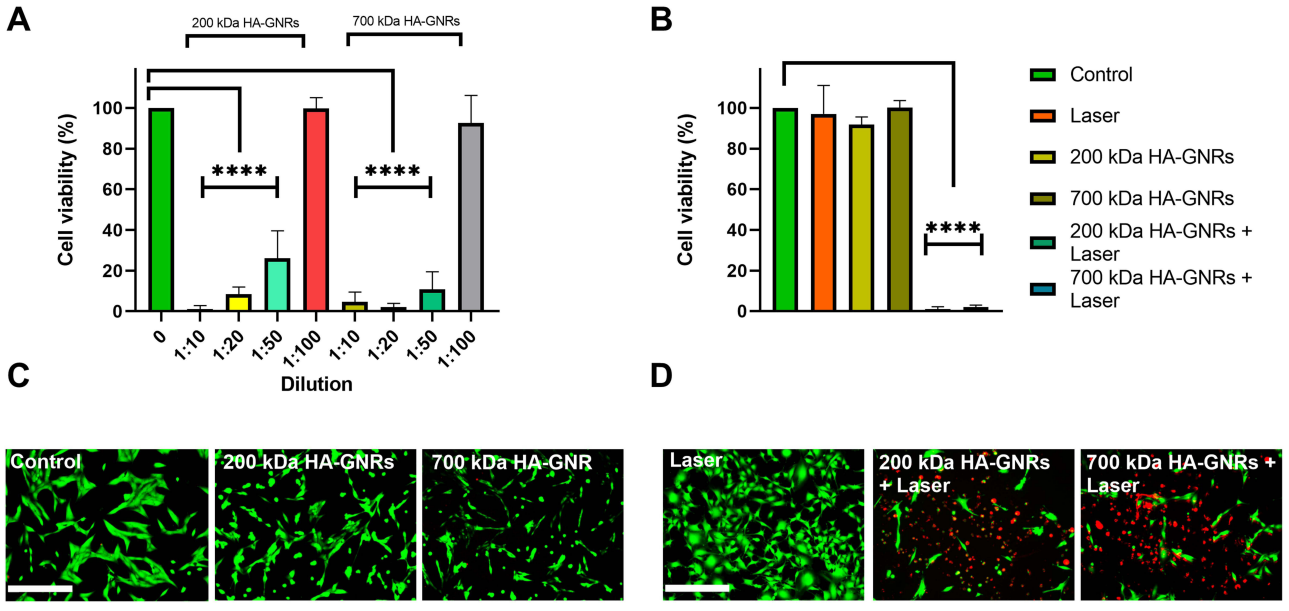

Figure 5 CT2A viability evaluated by XTT test 24h after incubation with decreasing dilutions of 200kDa-HA-GNRs and 700kDa-HA-GNRs (**A**) and 24h after irradiation with an 808nm laser for 10 minutes at 4,5W using HA-GNRs at 1:100 (**B**). Cell viability was also assessed by the Calcein-PI assay in CT2A cells after incubation with HA-GNRs at 1:100 (**C**) and after PTT treatments (**D**). Viable cells are shown in green and death cells in red. ****p<0.001. Scale bar: 200μm.

assays in both in vitro and in vivo experiments. Regarding in vitro PTT treatments (Figure 5B and D), no decrease in cell viability was observed when CT2A cells were treated either with the laser alone or incubated with HA-GNRs for 24 hours. The 808 nm laser was applied at 4.5W for 10 min without inducing any toxic effects on the CT2A cells, as described previously.[18] However, when the laser was applied to CT2A cells that had been incubated with both types of HA-GNRs, most cells in the culture were eliminated, as evidenced by XTT (Figure 5B) and calcein/PI (Figure 5D) assays. These results proved the effectiveness of both types of GNRs in inducing hyperthermia after laser irradiation and demonstrated their potential use as mediators for PTT treatments. Although both types of HA-GNRs were effective in promoting hyperthermia in response to laser irradiation, only 700 KD HA-GNRs were selected for in vivo PTT experiments due to the anticancer properties associated with this molecular weight HA.

In vivo PTT Treatments Tumor Volumetry

The efficacy of PTT treatment was also evaluated in vivo, in a mouse GBM model. Three different animal groups were analyzed to establish the in vivo efficiency of PTT: a control group consisting of untreated tumor-bearing mice, a GNR group consisting of tumor-bearing mice injected with HA-GNRs, and a PTT-treated group composed of tumor-bearing mice injected with HA-GNRs and irradiated with a laser, as described in the Material and Methods section. Tumor-bearing mice irradiated with the laser alone were not included in the in vivo PTT experiments, as we have previously demonstrated that laser irradiation using the same parameters as in the present study did not produce any effect on tumor size[32] and to align with the reduction principle of the 3Rs concept.[51] Additionally, the bioaccumulation of this type of GNRs has been previously evaluated, indicating that GNRs of similar size and composition to those used in this study did not exhibit any toxicity when injected intravenously.[52] Tumor size and tumor locations were analyzed by MRI one and two weeks after the PTT treatment (Figures 6 and 7).

One week after PTT treatments, untreated control animals showed much larger tumor masses (arrows in Figure 6A) compared to PTT-treated animals (arrows in Figure 6C), although not all tumor cells were eliminated in the treated animals. Therefore, the remaining tumor cells continued to grow over time. Consequently, two weeks after PTT treatments, the tumors in PTT-treated mice were again easily detectable by MRI (arrows in Figure 6D) and exhibited a larger size compared to the same condition one week after PTT treatment (arrows in Figure 6C). However, despite this increase, 15 days after the treatment, the tumor size of PTT-treated mice was significantly smaller than that of control mice (Figure 6B).

Tumor volume from all MRIs was quantified, as described above in the Materials and Methods section. The analysis showed that one week after PTT treatments, animals treated with laser following GNR injection exhibited a significantly smaller tumor size compared to control animals (Figure 7A), as can also be clearly observed in Figure 7E (PTT-treated mouse) compared to 7D (untreated mouse). PTT-treated animals also showed a smaller tumor size compared to animals treated solely with GNRs (Figure 7A). Similar results were observed 15 days after PTT treatments (Figure 7B), where the tumor sizes of PTT-treated animals were significantly smaller than those of untreated control mice. However, at this time post-PTT treatments, as mentioned before, tumor sizes were larger in all the groups tested.

Survival analyses were also conducted to assess the effectiveness of PTT. The Kaplan-Meier diagram in Figure 7C illustrates the percentage of mice alive at each time point following PTT treatments for the three different groups. Animals in all groups were euthanized upon the appearance of clear symptoms of stress and distress, in accordance with guidelines for the application of humane endpoints in distress situations in distress in laboratory animals.[53] Results indicated that untreated control mice and HA-GNR-injected mice had to be euthanized before reaching day 18 (counted after the last PTT treatment was applied to the PTT-treated group), due to a lack of motor capacity, which hindered their ability to eat or drink, or when their exploratory capacity was impaired, as indicated by the results of the open-field behavior test. In contrast, all PTT-treated animals survived beyond the point at which animals in the other two groups (Control and HA-GNRs) needed to be sacrificed (Figure 7C), demonstrating better health conditions that can be attributed to the effectiveness of the PTT. The mean survival time for the control and HA-GNRs groups was 17 and 16 days, respectively, and none of these mice survived beyond 18 days. In comparison, six of eight mice (75%) in the PTT-treated group were still alive at day 29 post-irradiation, and four of eight (50%) have survived more than 30 days. Analysis with a logrank test revealed a significant improvement in survival with HA-GNR-mediated PTT ($P = 0.0003$.

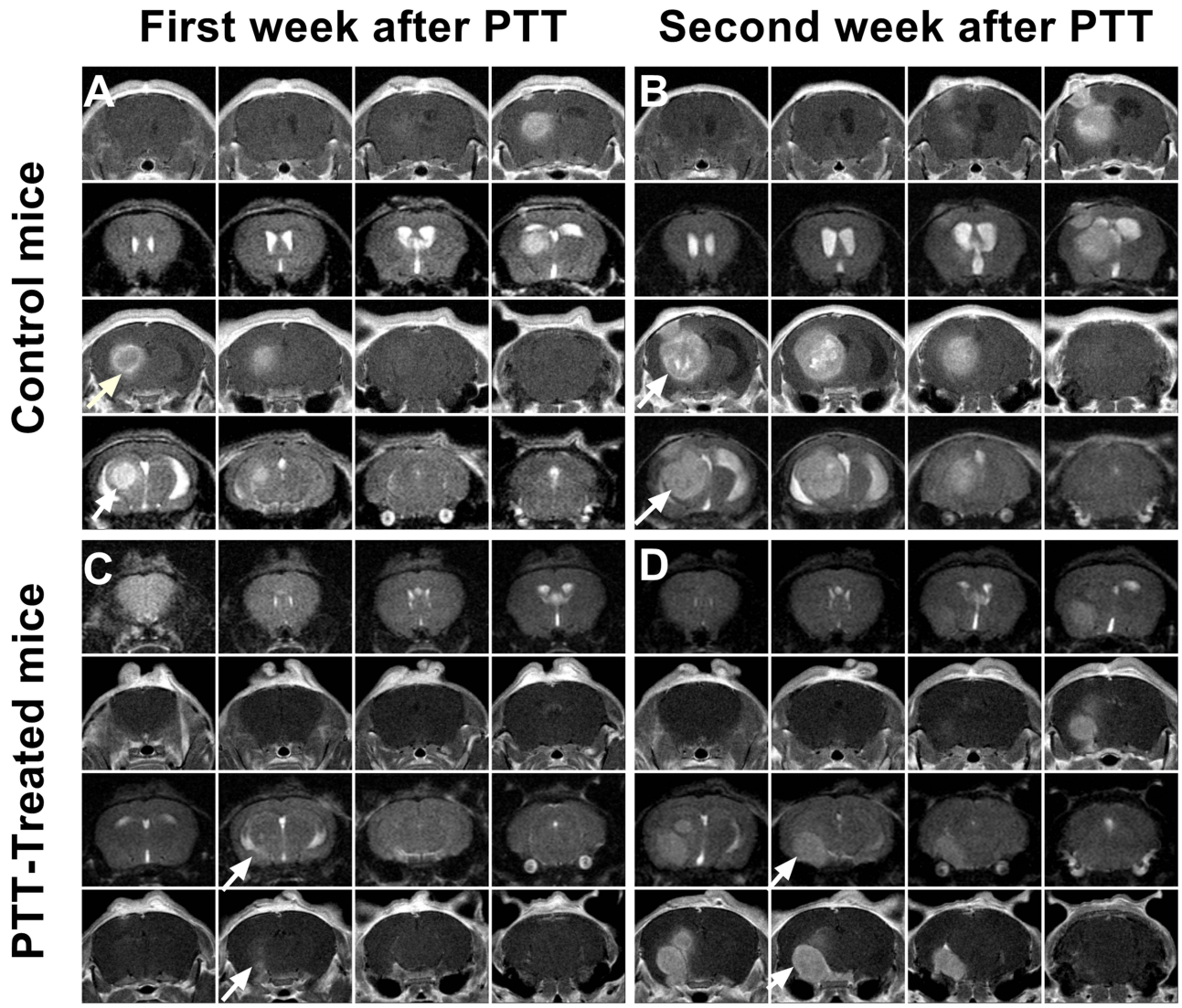

Figure 6 Serial MR images of tumor-bearing brains obtained from untreated (**A** and **B**) and PTT-treated (**C** and **D**) mice at 7- (**A** and **C**) and 15- (**B** and **D**) days after PTT application. White arrows indicate the location of the tumor mass.

p<0.001***). It can be concluded that HA-GNR-mediated PTT treatments have a significant influence on survival time. Tumors progressed rapidly, especially in the control group, where none of the five mice could be kept alive beyond day 18 (mean survival = 17 days). Similarly, HA-GNR mice showed a mean survival of 16 days, a period significantly lower than that of PTT-treated mice, which showed a mean survival period of 29.5 days.

Open Field Test

The Open Field test is a simple sensorimotor assay used to determine general activity levels, gross locomotor activity, and exploration habits in pathological mouse models affecting the central nervous system.[54] This behavioral test was performed two weeks after completing the PTT treatments. Distance moved and average speed during a 10-minute period were analyzed in the control group, HA-GNRs group, and PTT-treated group. PTT-treated mice exhibited intense exploratory behavior compared to untreated control mice, which showed a lack of exploratory ability (Figure 8A and B). Heat and trajectory maps showed that mice in the PTT-treated group displayed optimal motor and exploration capacity (upper panels in Figure 8C and D), while untreated control mice remained in the same place within the cages for longer periods (lower panels in Figure 8C and D).

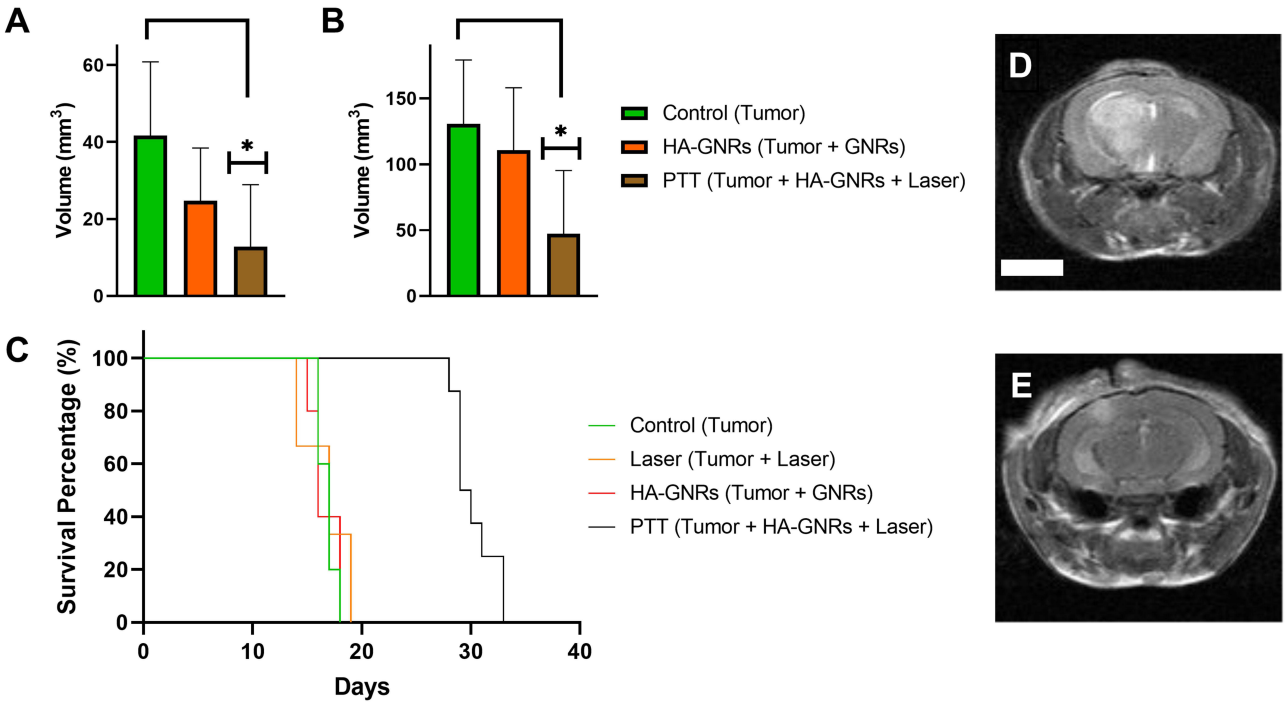

Figure 7 Tumor mass volumetry determined in the following tumor-bearing mouse groups: control (untreated), HA-GNRs and PTT-treated mice at 7 days (**A**) and 15 days (**B**) after PTT application. The Kaplan–Meier survival curve shows the evolution of the survival rate of the mouse population in each group over time (**C**). Individual MR images of untreated (**D**) and PTT-treated mice (**E**) one week after PTT treatment. Scale bar: 4mm. *p<0,05.

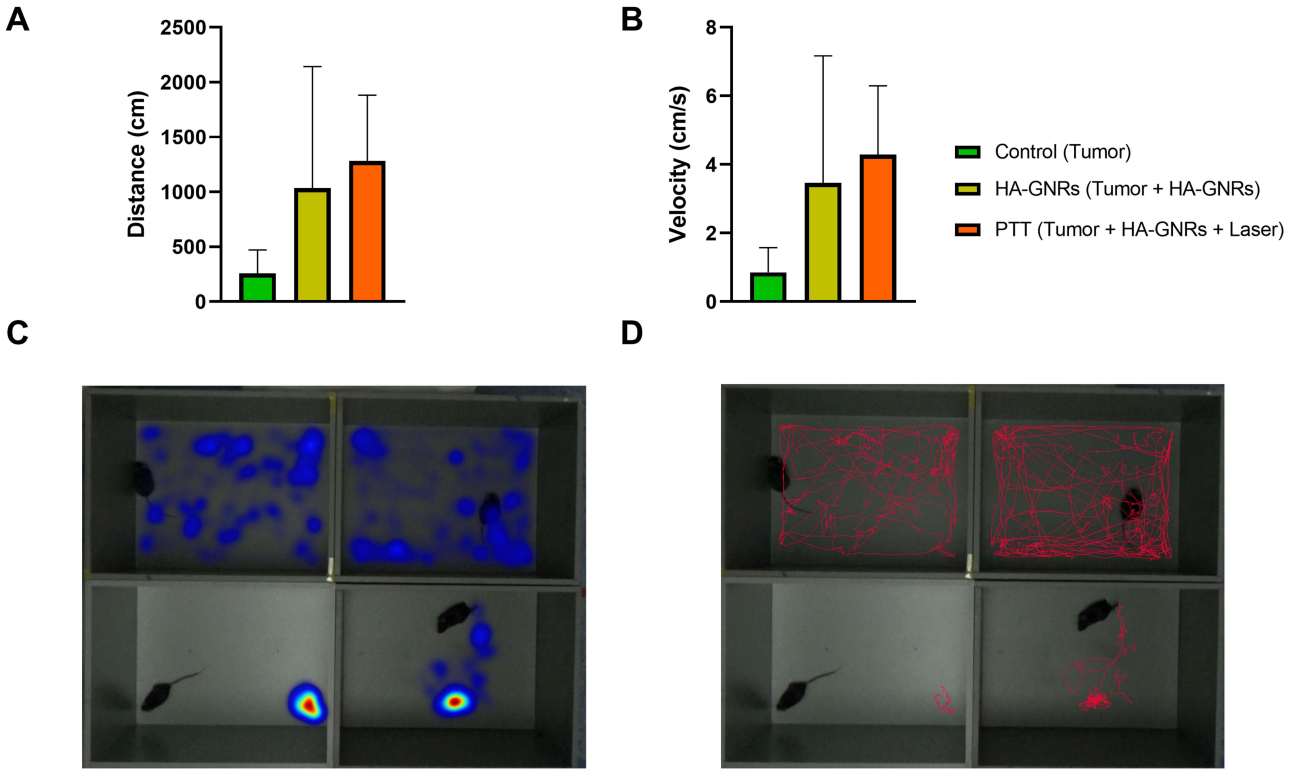

Figure 8 Assessment of general mouse activity using the open field test evaluated 15 days after PTT treatments. Distance traveled (**A**) and average speed (**B**) for control, HA-GNR, and PTT-treated mice are shown. Heat maps (**C**) indicate the time spent in each zone, and red lines (**D**) represent the trajectories followed by PTT-treated (upper panels) and control (lower panels) mice.

https://doi.org/10.2147/IJN.S525462

Histological Analysis

In order to assess the effectiveness of PTT at cellular level, histological analyses were conducted using immunofluorescence assays. Implanted CT2A cells can be readily distinguished by nestin and Iba1 staining.[55,56] Consequently, the tumor area can be easily identified by positive staining for nestin (Figure 9A) and Iba1 (Figure 9F). The tumor mass can also be identified by a high density of nuclei, labeled with Hoechst, in comparison to the surrounding brain tissue (Figure 9B and G). The nestin fluorescence signal matched the high density of nuclei revealed by Hoechst, delineating the tumor area (Figure 9A–C and E), whereas no nestin labeling was observed outside the tumor area (Figure 9D).

Iba1 is a well-established marker for microglia staining, which is upregulated during their activation.[57] In this tumor model, cells outside the tumor labeled with an anti-Iba1 antibody exhibited a stellated morphology (Figure 10A–C), whereas Iba1-positive cells within the tumor tissue present a smaller size with a round or amoeboid morphology (Figure 10D–F), indicative of the activation of these cells within the tumor tissue.[56] Microglial cells are attracted towards tumor tissue, resulting in enhanced Iba1 staining, which is highly useful for delineating the limits of the tumor tissue (Figure 10G–I).

Due to all these features, the tumor tissue was accurately localized and delineated by labeling with Iba1, nestin, and Hoechst in all the sections analyzed.

The effects of PTT treatments can also be determined by histological analyses, as evidenced by an apoptotic marker. CT2A cells present in the tumor area in PTT-treated mouse brain sections exhibited a strong signal when labeled with an anti-cleaved-caspase 3 antibody (Figure 11I and J), a marker of apoptotic cell death. This indicates that CT2A tumor cells

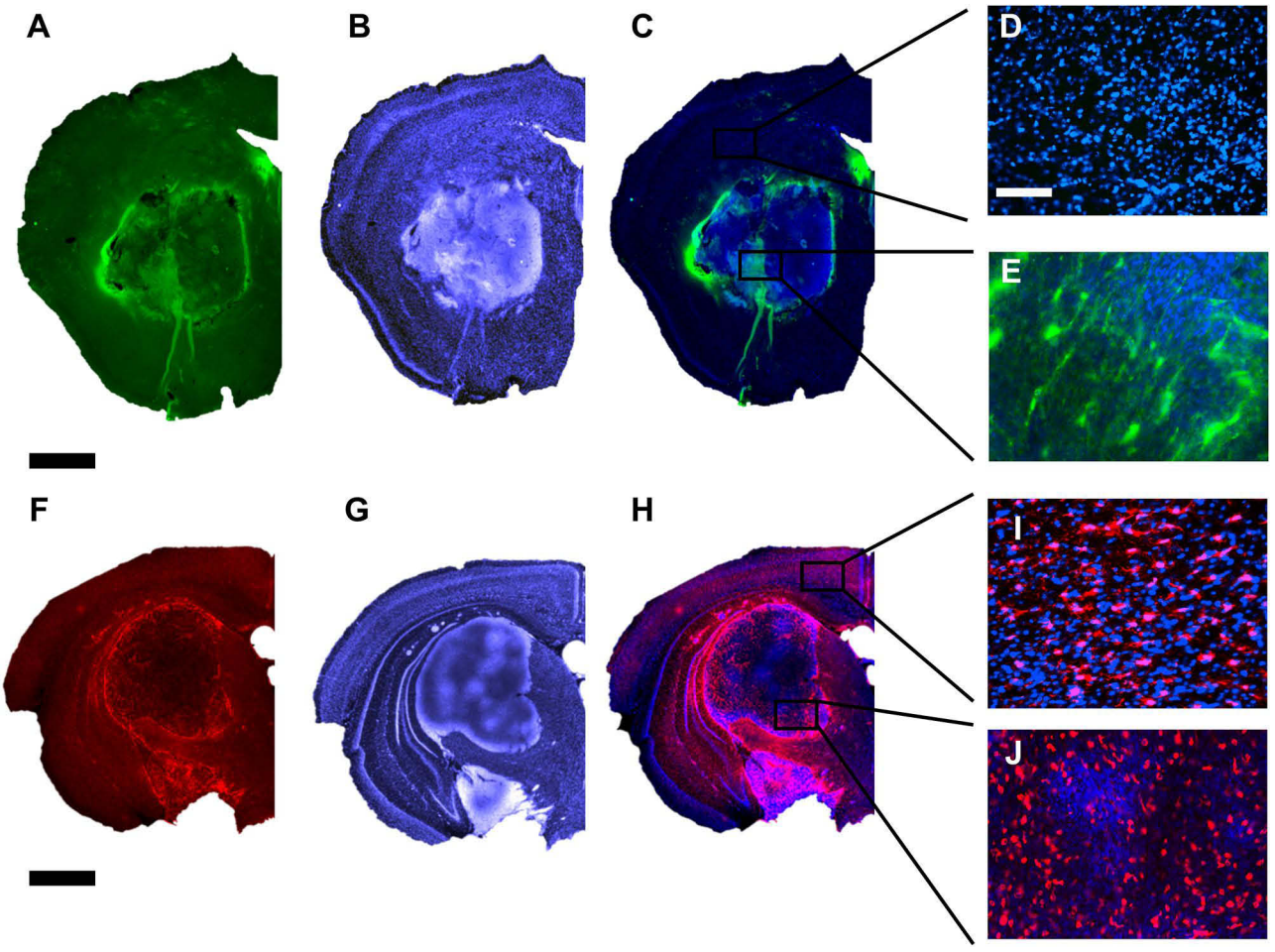

Figure 9 Representative images of coronal brain sections obtained from control untreated tumor bearing mouse, showing the localization of the implanted CT2A cells labeled with an antibody anti-nestin in green (**A**–**E**), and an antibody anti-Iba1 in red (red) (**F**–**J**). Nuclei were counterstained with Hoechst in blue (**B** and **G**). Merged images of (**A, B** and **F**–**G**) are shown in (**C** and **H**), respectively. Boxed areas in (**C** and **H**) are shown at higher magnification in (**D**–**E**) and (**I**–**J**), respectively. Scale bars in (**A**) and (**F**) 800 μm (valid for (**A**–**C**) and (**F**–**H**). Scale bars in (**D**) 100 μm (valid for **D, E, I** and **J**).

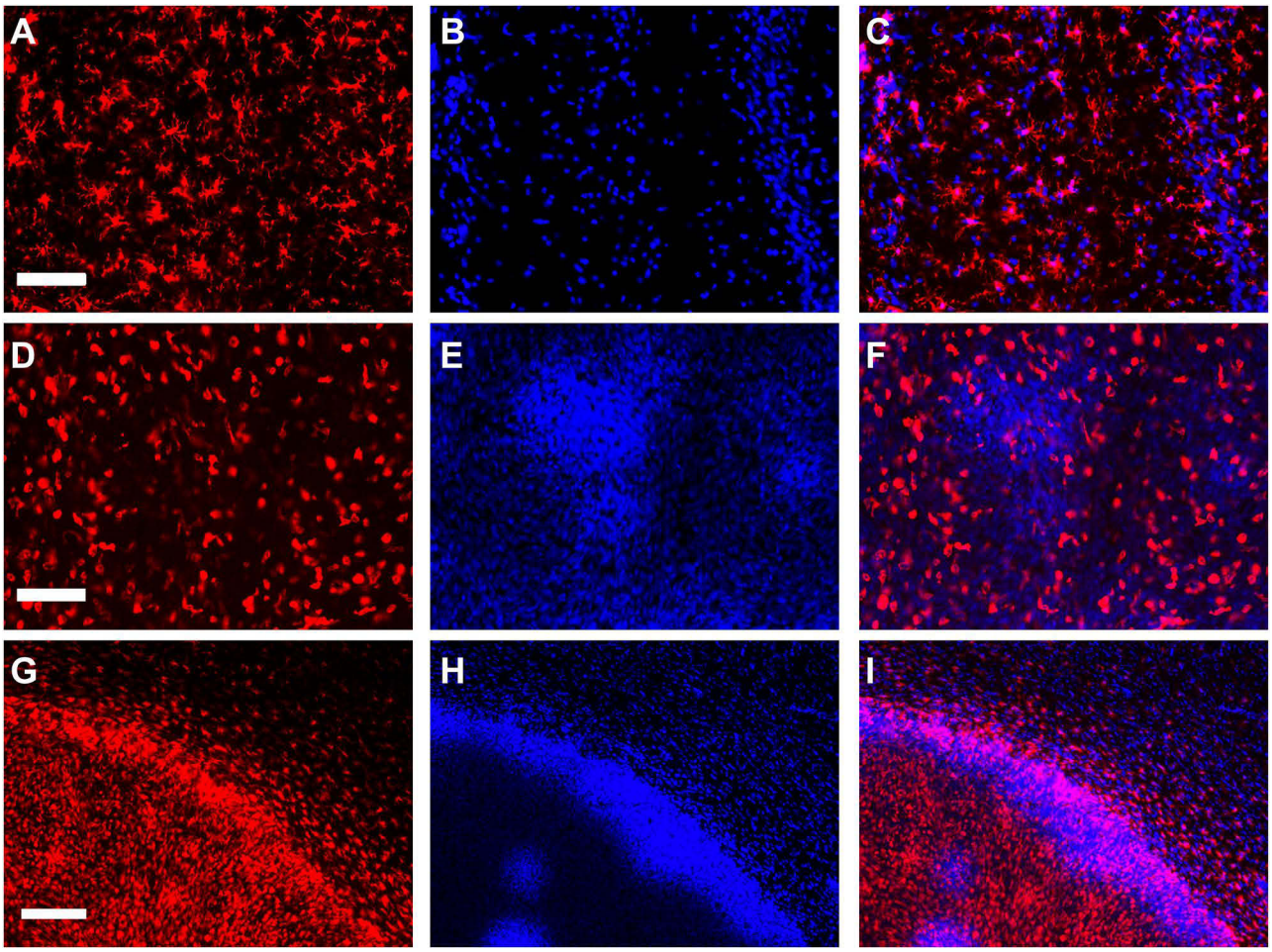

Figure 10 Representative images of brain sections from a control tumor-bearing mouse, showing the localization limits of CT2A tumor cells by immunofluorescence using anti-Iba1 (red) staining (**A, D** and **G**) in three different locations: outside the tumor (**A**–**C**), inside the tumor (**D**–**F**), and at the boundary of the tumor (**G**–**I**). Nuclei were counterstained in blue with Hoechst labeling (**B, E** and **H**). Merged images of (**A, B, D, E** and **G, H**) images are shown in (**C, F** and **I**), respectively. Scale bar for (**A**–**F**) 100 μm, scale bar for (**G**–**I**): 200 μm.

underwent apoptotic processes in response to laser irradiation in the presence of HA-GNRs. However, apoptotic cells were not observed in the tumor tissue of the untreated mouse brain sections (Figure 11D and E).

Discussion

PTT mediated by gold nanoparticles locally increases the temperature to 41–46 °C leading to sensitization, heat responses, denaturalization and apoptosis of cancer cells.[22,58] GNRs possess the most efficient nanoparticle shape for heat conversion due to their high absorption in the near-infrared region.[59]

One advantage of GNRs is their well-defined synthesis, which allows for the modulation of their shape and aspect ratio through specific seeded growth methods. The dimensions of the GNRs produce two absorption peaks known as longitudinal and transverse plasmon resonance.[60,61] Due to their anisotropic shape, GNRs demonstrate a longer circulation period in the blood compared to other types of gold nanoparticles such as nanocages or nanospheres.[62] In a comparison between rod-shaped and spherical nanoparticles, GNRs exhibit higher tumor targeting efficiency and longer tumor retention time, while nanospheres offer better renal clearance.[63] In addition, heat conversion efficiency is superior in GNRs compared to nanospheres because, once internalized by cancer cells, the proximity between the nanoparticles enhances their effectiveness. However, nanospheres are affected by endosomal confinement inside the cells.[64,65]

https://doi.org/10.2147/IJN.S525462

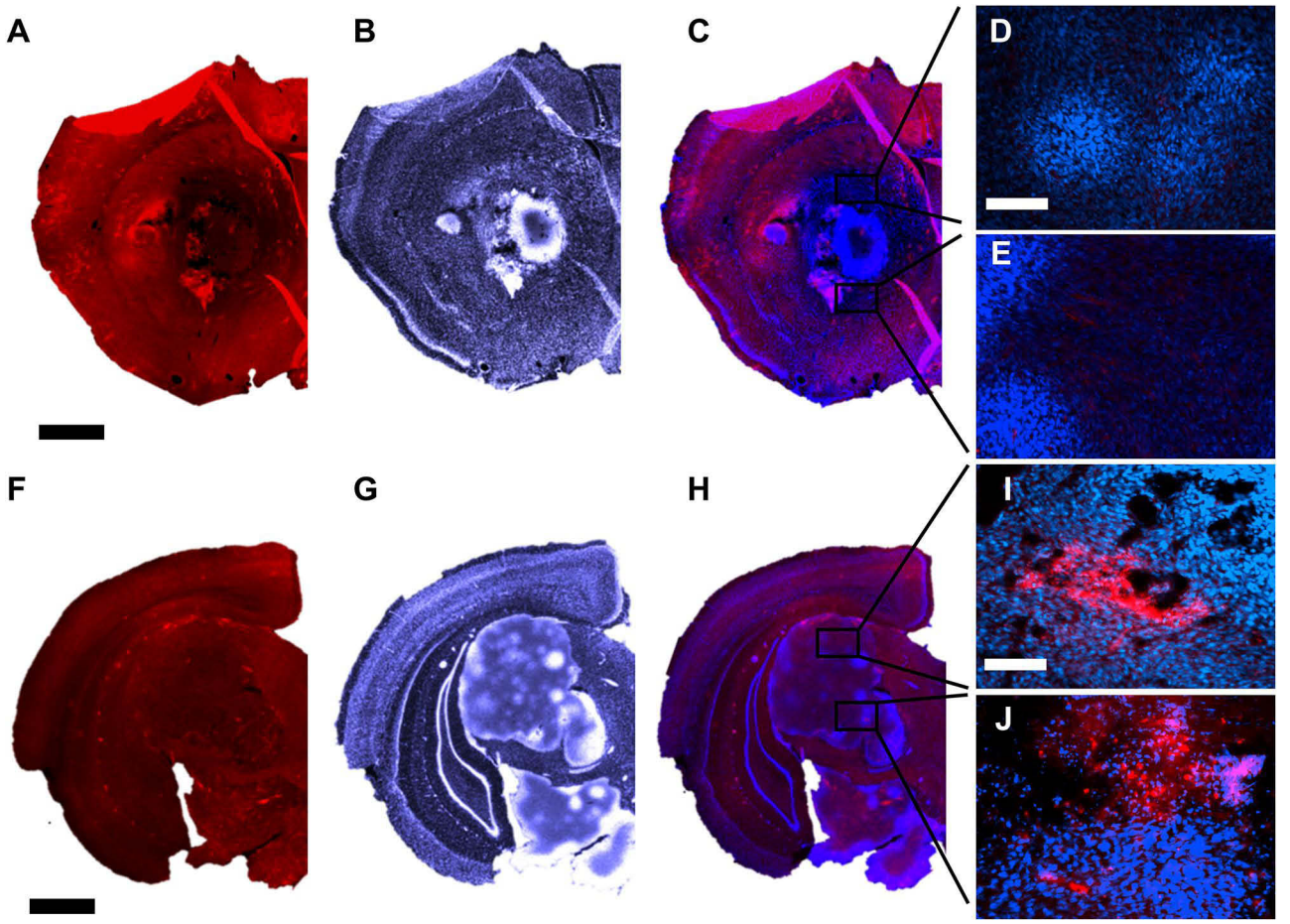

Figure 11 Representative images of coronal brain sections from the right hemisphere of tumor-bearing mice: control (**A–E**) and PTT-treated (**F–J**), stained in red with an anti-cleaved caspase 3 antibody to mark apoptotic cells (**A** and **F**). Nuclei were counterstained with Hoechst in blue (**B** and **G**). Merged images of A and B, and F and G, are shown in C and H, respectively. Boxed areas in (**C**) and (**H**) are shown at higher magnification in (**D, E**) and (**I, J**), respectively. Scale bars for (**A–C**) and (**F–H**): 800 μm; scale bars for (**D, E**) and (**I, J**): 200 μm.

The method of synthesis and biofunctionalization of the GNRs, along with their shape, size, concentration, and the type of cell used, are critical parameters for achieving lower rates of cytotoxicity and facilitating the internalization of the nanoparticles by the cells.[66,67] In the synthesis of GNRs, the cationic surfactant cetyltrimethylammonium bromide (CTAB) is used to form rod-like micelles in aqueous solution.[68] However, the biocompatibility of GNRs can be compromised by the presence of CTAB or other residual chemicals used during particle synthesis. Therefore, adding a polymeric coating or a layer of biomolecules to the surface of GNRs reduces their cytotoxicity.[69] In this work, GNRs were biofunctionalized with HA of different molecular weights: 200 and 700 kDa. HA is a biomolecule used in GNR biofunctionalization for its antiproliferative effects in solid tumors, including GBM.[70] The cytotoxic profiles of both types of HA-GNRs were similar when incubated with CT2A cells. In addition, the effects of PTT in the presence of each type of particle demonstrated the effectiveness of both types of GNR in eliminating cancer cells. These results are consistent with those described in the literature[71,72] which showed that HA-based nanoparticles have a non-cytotoxic effect on cancer cells and are effective in PTT, even when HA of different molecular weights was used to biofunctionalized the GNRs.[42]

A glioblastoma mouse model was used to evaluate the efficacy of HA-GNRs in PTT. This model is commonly used to evaluate various anti-tumor treatments for GBM.[73–75] The injected CT2A cells form a homogeneous hypercellular mass with well-defined borders but exhibit a highly infiltrative pattern, leading to satellite lesions within the brain. CT2A tumors are characterized by high cell density, significant mitotic activity, angiogenesis, microvascular proliferation, and spontaneous hemorrhage.[49] Some of these features were confirmed by immunohistochemistry, validating the malignant

nature of the injected CT2A cells. In addition, CT2A glioma cells are pleomorphic, with large fusiform and small round shapes and prominent nuclei.[38] The abundant interstitial space between cells indicates an interstitial alteration within the tumor, another characteristic of CT2A tumors.

CT2A cells, like many other cancer cell lines, overexpress the CD44 protein on their membrane, which serves as the receptor for HA. This receptor is responsible for various functions in tumor cells, including increased cell invasion ability, enhanced proliferation through the induction of growth pathways, inhibition of tumor suppressors, and resistance to chemoradiation.[34,76,77] To specifically target CT2A cells and enhance the effectiveness of PTT, GNRs biofunctionalized with HA, the ligand for the CD44 receptor, were used in this study. Scientific evidence indicates that HA biofunctionalization enhances blood circulation time and promotes the accumulation of nanoparticles in tumors.[78,79] This effect has also been observed when using nanoparticles as drug delivery systems in combination with PTT,[80] or when nanodevices, such as mesoporous nanoparticles, were employed as theranostic carriers.[81]

In this study, HA of 700 kDa has been selected for biofunctionalizing GNRs due to its antiproliferative and antiangiogenic effects, its ability to activate the immune system, and its efficient uptake by cancer cells.[42] This work demonstrates the effectiveness of the method to eliminate cancer cells, as we observed a reduction in tumor mass in tumor-bearing mice treated with PTT following HA-GNRs injection, compared to control mice. Volumetric MRI analyses indicated that the reduction in tumor mass volume in PTT-treated mice remained evident even two weeks after laser irradiation. These results are consistent with studies that have shown the effectiveness of HA in targeting GBM cells using HA-micelles.[82]

In many published studies, the effect of PTT on GBM cells has been evaluated using heterotopic GBM models, where tumor cells are injected into the flank of the animal, facilitating easier, but unrealistic, laser irradiation.[83,84] However, in this study, we assess the viability of the PTT using an orthotopic model, which more accurately reflects the clinical scenario. The effect of the PTT has been evaluated through volumetric MRI analyses, as previously established,[83] revealing the positive impact of PTT in reducing tumor volume in PTT-treated animals. Additionally, this orthotopic model induces brain damage that affects the locomotor system and the exploratory capacity of the animals.[49] These impairments can be assessed using appropriate behavioral tests, such as the open field test, allowing for a more precise determination of the PTT effectiveness. These tests revealed that the PTT-treated animals exhibited greater locomotor activity, covering longer distances at a higher speed compared to the untreated animals, confirming the effectiveness of the HA-GNR-mediated PTT.

Recent studies have revealed the role of nestin in tumor cells, highlighting its involvement in mitotic progression and identifying it as a potential target for microtubule-destabilizing drugs.[55] Nestin is upregulated in GBM tissues compared to low-grade gliomas, as we have confirmed (Figure 9). Therefore, nestin might be considered a promising ligand for targeting GBM cells. It has been utilized to biofunctionalize GNRs for PTT of GBM, demonstrating high uptake by cancer cells and producing a significant percentage of cell death after PTT treatment.[33,85]

In the GBM model presented here, CT2A cells formed nestin-positive tumor masses, which corresponded very precisely with areas of high cellular density revealed by Hoechst staining, as shown in Figure 9. This characteristic makes this model suitable for testing new targets, such as nestin, to biofunctionalize GNRs for PTT of GBM.

The state of microglia in this GBM model was analyzed using Iba1 immunohistochemistry. Outside the tumor area, microglia exhibited a ramified phenotype, which is involved in synapse pruning, surveillance, and maintaining cellular homeostasis.[56] However, within the tumor, the phenotype shifted to an amoeboid shape, indicating activated, rounded cells without ramification, which are associated with metastases and intracranial bleeding.[56]

The activation of microglia primarily occurs through Toll-like receptor-4 (TLR4). Microglial cell activation is classified into two phenotypes: M1 and M2. The M1 phenotype is characterized by the production of pro-inflammatory cytokines and neurotoxic activity, while the M2 phenotype, activated by apoptosis signals, plays a role in remodeling and repair.[57] These microglial phenotypes align with the characteristics of the GBM model used, which is known for its hemorrhagic and infiltrative nature.[32] As shown in Figures 9 and 10, the microglial cells within the tumor adopt an ameboid form. Consequently, Iba1 staining can serve as an additional tool to delineate the tumor boundaries. This microglial staining pattern correlates well with the nestin marker and the high-intensity Hoechst labeling, which indicates a high number of nuclei.

HA modulates inflammation in the central nervous system, with high molecular weight HA (>500 kDa) exerting anti-inflammatory effects, while low molecular weight HA exhibits pro-inflammatory effects on myeloid cells,

including microglia.[86] In these terms, astrocytes also modulate inflammation,[87] however the link between HA and astrocytes is very complex and it needs further investigations. Some studies[87,88] report the anti-inflammatory function of high MW-HA molecules, such as those used in this study to functionalize the GNRs, through TLR4 modulation. Additionally, 700 kDa HA-coated GNRs specifically targeted CT2A cells over other brain cells due to the higher expression of CD44 in tumor cells, as previously described.[89] The specificity of 700 kDa HA-coated GNRs to target GBM cells over other brain cell types, combined with its anti-inflammatory effects, makes high MW-HA an ideal biomolecule to attach to the surface of nanoparticles for PTT and other strategies, such as drug nanocarriers, micelles, or liposomes, to treat GBM.

It has been shown that PTT can modulate cellular death pathways, leading to either apoptosis or necrosis depending on the temperature achieved during the treatment. The induction of apoptosis or necrosis is influenced by several PTT parameters, including laser power, irradiation time, and GNR concentration. The apoptotic cell death induced by GNR-based PTT is crucial, as apoptosis can trigger beneficial immunogenic responses and reduce the risk of secondary tumor formation.[90] Apoptosis activation in GBM cells by in vitro PTT was also demonstrated by other studies,[18,91,92] some of which were conducted by our research group. In these previous studies, PTT-induced apoptosis was produced by different sizes of PEG-GNRs, without a target specificity, and was accompanied by lysosomal rupture that ultimately activated the apoptotic mechanism. However, the mechanism of action of these non-biofunctionalized GNRs was only tested in in vitro experiments using glioblastoma cell lines. The novelty of the present study lies in demonstrating that, in the in vivo GBM model described, the applied PTT parameters induced tumor cell death, at least partially through apoptotic pathways. This significant tumor cell death was accompanied by an improvement in the animals' behavior, as assessed by their exploratory capacity.

The reduction in tumor mass observed after PTT can be partially attributed to the effect of HA-GNRs on CT2A cells, as tumor-bearing mice injected with HA-GNRs but without laser irradiation also showed a partial decrease in tumor volume. This effect may be due to the ability of HA to inhibit cell proliferation,[70,93] since the injection of non-functionalized GNRs into a similar GBM mouse model did not result in a decrease in tumor mass under the same conditions.[32]

Although HA-GNR-based PTT in our GBM model has a limited effect on completely eliminating tumor cells, there is room for improvement, as the laser irradiation applied in this study was underpowered compared to other studies,[94,95] and repeated laser applications can be considered, as GNRs remain in the area where they are injected. Additionally, this HA-GNR-based PTT can be combined with other classical therapies, such as chemotherapy, to improve its therapeutic effects. The heat generated by GNR-based-PTT enhances the permeability of leaky tumor vessels, facilitating the accumulation of chemotherapeutic drugs.[90]

Conclusion

This study demonstrates the efficacy of the newly developed HA-GNRs for PTT applications in eliminating CT2A cells in an in vivo GBM model. HA-GNR-mediated PTT resulted in a significant reduction in tumor mass, as assessed by MRI, along with improved exploratory behavior and extended life expectancy in the treated animals, confirming in vivo tumor regression. HA-GNR-mediated PTTs induced cell death via apoptotic mechanisms, potentially enhancing the immune system's ability to target and eliminate residual tumor cells.

Abbreviations

FBS, Fetal bovine serum; GBM, Glioblastoma Multiforme; GCSC, Glioblastoma Cancer Stem Cells; GNRs, Gold Nanorods; HA, Hyaluronic Acid; IDH, Isocitrate Dehydrogenase; LSPR, Localized Surface Plasmon Resonance; MRI, Magnetic Resonance Imaging; MW, Molecular Weights; NIR, Near Infrared; NPs, Nanoparticles; PI, Propidium Iodide; PTT, Nanoparticle-mediated Photothermal Therapy; RES, Reticuloendothelial System; XTT, 2,3-bis-(2-methoxy-4-nitro-5-sulfophenyl)-2H-tetrazolium-5-carboxanilide salt.

Acknowledgments

The authors would like to thank Soledad Martinez for the excellent technical assistance. This study was partially funded by the Ministerio de Ciencia, Innovación y Universidades of Spain, Refs.: PGC2018-097531-B-I00, PID2022-

138881OB-I00 and PDC2022-133028-I00, funded by the European Union-NextGenerationEU. CS acknowledges the financial supported by MUR in the framework of PRIN2022-PNRR call under project CoMu4CaT. The abstract of this paper was presented at the 7th Spanish Conference on Biomedical Applications of Nanomaterials (SBAN).

Disclosure

The authors report no conflicts of interest in this work.

References

1. Tan AC, Ashley DM, López GY, Malinzak M, Friedman HS, Khasraw M. Management of glioblastoma: state of the art and future directions. *CA Cancer J Clin*. 2020;70(4):299–312. doi:10.3322/caac.21613
2. Louis DN, Perry A, Wesseling P, et al. The 2021 WHO classification of tumors of the central nervous system: a summary. *Neuro Oncol*. 2021;23(8):1231–1251. doi:10.1093/neuonc/noab106
3. Gritsch S, Batchelor TT, Gonzalez Castro LN. Diagnostic, therapeutic, and prognostic implications of the 2021 World Health Organization classification of tumors of the central nervous system. *Cancer*. 2022;128(1):47–58. doi:10.1002/cncr.33918
4. Dimov I, Tasić-Dimov D, Conić I, Stefanovic V. Glioblastoma multiforme stem cells. *Sci World J*. 2011;11:930–958. doi:10.1100/tsw.2011.42
5. Weller M, Wick W, Aldape K, et al. Glioma. *Nat Rev Dis Primers*. 2015;1(15017). doi:10.1038/nrdp.2015.17
6. Czarnywojtek A, Borowska M, Dyrka K, et al. Glioblastoma Multiforme: the Latest Diagnostics and Treatment Techniques. *Pharmacology*. 2023;108(5):423–431. doi:10.1159/000531319
7. Omuro A, DeAngelis LM. Glioblastoma and other malignant gliomas: a clinical review. *JAMA*. 2013;310(17):1842–1850. doi:10.1001/jama.2013.280319
8. Davis ME. Epidemiology and Overview of Gliomas. *Semin Oncol Nurs*. 2018;34(5):420–429. doi:10.1016/j.soncn.2018.10.001
9. Alifieris C, Trafalis DT. Glioblastoma multiforme: pathogenesis and treatment. *Pharmacol Ther*. 2015;152:63–82. doi:10.1016/j.pharmthera.2015.05.005
10. Liu S, Shi W, Zhao Q, et al. Progress and prospect in tumor treating fields treatment of glioblastoma. *Biomed. Pharmacother*. 2021;141:111810. doi:10.1016/j.biopha.2021.111810
11. Regli LKP, Huijs SMH, Pasmans RCOS, et al. Incidence of clinically relevant psychiatric symptoms during glioblastoma treatment: an exploratory study. *J Neurooncol*. 2023;163(1):185–194. doi:10.1007/s11060-023-04326-2
12. Huang B, Li X, Li Y, Zhang J, Zong Z, Zhang H. Current Immunotherapies for Glioblastoma Multiforme. *Front Immunol*. 2021;11:603911. doi:10.3389/fimmu.2020.603911
13. Gawel AM, Singh R, Debinski W. Metal-Based Nanostructured Therapeutic Strategies for Glioblastoma Treatment—An Update. *Biomedicines*. 2022;10(7):1598. doi:10.3390/biomedicines10071598
14. Carlsson SK, Brothers SP, Wahlestedt C. Emerging treatment strategies for glioblastoma multiforme. *EMBO Mol Med*. 2014;6(11):1359–1370. doi:10.15252/emmm.201302627
15. Zhi D, Yang T, O'Hagan J, Zhang S, Donnelly RF. Photothermal therapy. *J Control Release*. 2020;325:52–71. doi:10.1016/j.jconrel.2020.06.032
16. Kong C, Chen X. Combined Photodynamic and Photothermal Therapy and Immunotherapy for Cancer Treatment: a Review. *Int J Nanomed*. 2022;17:6427–6446. doi:10.2147/IJN.S388996
17. Gupta N, Malviya R. Understanding and advancement in gold nanoparticle targeted photothermal therapy of cancer. *Biochim Biophys Acta Rev Cancer*. 2021;1875(2):188532. doi:10.1016/j.bbcan.2021.188532
18. Domingo-Diez J, Souiade L, Manzaneda-González V, et al. Effectiveness of Gold Nanorods of Different Sizes in Photothermal Therapy to Eliminate Melanoma and Glioblastoma Cells. *Int J Mol Sci*. 2023;24(17):13306. doi:10.3390/ijms241713306
19. Li C, Cheng Y, Li D, et al. Antitumor Applications of Photothermal Agents and Photothermal Synergistic Therapies. *Int J Mol Sci*. 2022;23(14):7909. doi:10.3390/ijms23147909
20. Hou YJ, Yang XX, Liu RQ, et al. Pathological mechanism of photodynamic therapy and photothermal therapy based on nanoparticles. *Int J Nanomed*. 2020;15:6827–6838. doi:10.2147/IJN.S269321
21. Shang T, Yu X, Han S, Yang B. Nanomedicine-based tumor photothermal therapy synergized immunotherapy. *Biomater Sci*. 2020;8(19):5241–5259. doi:10.1039/d0bm01158d
22. Vines JB, Yoon JH, Ryu NE, Lim DJ, Park H. Gold nanoparticles for photothermal cancer therapy. *Front Chem*. 2019;7:167. doi:10.3389/fchem.2019.00167
23. Naletova I, Cucci LM, D'Angeli F, et al. A tunable nanoplatform of nanogold functionalised with Angiogenin peptides for anti-angiogenic therapy of brain tumours. *Cancers (Basel)*. 2019;11(9):1322. doi:10.3390/cancers11091322
24. Hu X, Zhang Y, Ding T, Liu J, Zhao H. Multifunctional Gold Nanoparticles: a Novel Nanomaterial for Various Medical Applications and Biological Activities. *Front Bioeng Biotechnol*. 2020;8:990. doi:10.3389/fbioe.2020.00990
25. Tomasella P, Sanfilippo V, Bonaccorso C, et al. Theranostic nanoplatforms of thiolated reduced graphene oxide nanosheets and gold nanoparticles. *Appl Sci*. 2020;10(16):5529. doi:10.3390/app10165529
26. Kesharwani P, Chadar R, Sheikh A, Rizg WY, Safhi AY. CD44-Targeted Nanocarrier for Cancer Therapy. *Front Pharmacol*. 2022;12:800481. doi:10.3389/fphar.2021.800481
27. Liu J, He H, Xiao D, et al. Recent advances of plasmonic nanoparticles and their applications. *Materials*. 2018;11(10):1833. doi:10.3390/ma11101833
28. Foti A, Calì L, Petralia S, Satriano C. Green Nanoformulations of Polyvinylpyrrolidone-Capped Metal Nanoparticles: a Study at the Hybrid Interface with Biomimetic Cell Membranes and In Vitro Cell Models. *Nanomaterials*. 2023;13(10):1624. doi:10.3390/nano13101624
29. Norouzi M. Gold Nanoparticles in Glioma Theranostics. *Pharmacol Res*. 2020;156:104753. doi:10.1016/j.phrs.2020.104753
30. Dobrovolskaia MA, Patri AK, Zheng J, et al. Interaction of colloidal gold nanoparticles with human blood: effects on particle size and analysis of plasma protein binding profiles. *Nanomedicine*. 2009;5(2):106–117. doi:10.1016/j.nano.2008.08.001

31. Ludwig K, Kornblum HI. Molecular markers in glioma. *J Neurooncol*. 2017;134(3):505–512. doi:10.1007/s11060-017-2379-y
32. Casanova-Carvajal O, Urbano-Bojorge AL, Ramos M, Serrano-Olmedo JJ, Martínez-Murillo R. Slowdown intracranial glioma progression by optical hyperthermia therapy: study on a CT-2A mouse astrocytoma model. *Nanotechnology*. 2019;30(35):355101. doi:10.1088/1361-6528/ab2164
33. Gonçalves DPN, Rodriguez RD, Kurth T, et al. Enhanced targeting of invasive glioblastoma cells by peptide-functionalized gold nanorods in hydrogel-based 3D cultures. *Acta Biomater*. 2017;58:12–25. doi:10.1016/j.actbio.2017.05.054
34. Mooney KL, Choy W, Sidhu S, et al. The role of CD44 in glioblastoma multiforme. *J Clin Neurosci*. 2016;34:1–5. doi:10.1016/j.jocn.2016.05.012
35. Mesrati MH, Syafruddin SE, Mohtar MA, Syahir A. CD44: a multifunctional mediator of cancer progression. *Biomolecules*. 2021;11(12):1850. doi:10.3390/biom11121850
36. Mattheolabakis G, Milane L, Singh A, Amiji MM. Hyaluronic acid targeting of CD44 for cancer therapy: from receptor biology to nanomedicine. *J Drug Target*. 2015;23(7–8):605–618. doi:10.3109/1061186X.2015.1052072
37. Abatangelo G, Vindigni V, Avruscio G, Pandis L, Brun P. Hyaluronic acid: redefining its role. *Cells*. 2020;9(7):1–19. doi:10.3390/cells9071743
38. Binello E, Qadeer ZA, Kothari HP, Emdad L, Germano IM. Stemness of the CT-2A immunocompetent mouse brain tumor model: characterization in vitro. *J Cancer*. 2012;3(1):166–174. doi:10.7150/jca.4149
39. Kolliopoulos C, Ali MM, Castillejo-Lopez C, Heldin CH, Heldin P. CD44 Depletion in Glioblastoma Cells Suppresses Growth and Stemness and Induces Senescence. *Cancers (Basel)*. 2022;14(15):3747. doi:10.3390/cancers14153747
40. Doualle C, Gouju J, Nouari Y, et al. Dedifferentiated Cells Obtained from Glioblastoma Cell Lines Are an Easy and Robust Model for Mesenchymal Glioblastoma Stem Cells Studies. *Am J Cancer Res*. 2023;13(4):1425–1442. PMCID: PMC10164819.
41. Misra S, Heldin P, Hascall VC, et al. Hyaluronan-CD44 interactions as potential targets for cancer therapy. *FEBS J*. 2011;278(9):1429–1443. doi:10.1111/j.1742-4658.2011.08071.x
42. Sanfilippo V, Caruso VCL, Cucci LM, Inturri R, Vaccaro S, Satriano C. Hyaluronan-metal gold nanoparticle hybrids for targeted tumor cell therapy. *Int J Mol Sci*. 2020;21(9):3085. doi:10.3390/ijms21093085
43. Machado V, Morais M, Medeiros R. Hyaluronic Acid-Based Nanomaterials Applied to Cancer: where Are We Now? *Pharmaceutics*. 2022;14 (10):2092. doi:10.3390/pharmaceutics14102092
44. Chen JWE, Pedron S, Shyu P, Hu Y, Sarkaria JN, Harley BAC. Influence of Hyaluronic Acid Transitions in Tumor Microenvironment on Glioblastoma Malignancy and Invasive Behavior HHS Public Access. *Front Mater*. 2018;5:39. doi:10.3389/fmats.2018.00039
45. Salari N, Mansouri K, Valipour E, et al. Hyaluronic acid-based drug nanocarriers as a novel drug delivery system for cancer chemotherapy: a systematic review. *DARU J Pharma Sci*. 2021;29(2):439–447. doi:10.1007/s40199-021-00416-6
46. Tang X, Kurban M, Hafiz I, Shen Q, Wang M. Preparation of hyaluronic acid-loaded Harmine polymeric micelles and in vitro effect anti-breast cancer. *Eur J Pharm Sci*. 2023;183:106388. doi:10.1016/j.ejps.2023.106388
47. Berridge MV, Herst PM, Tan AS. Tetrazolium dyes as tools in cell biology: new insights into their cellular reduction. *Biotechnol Annu Rev*. 2005;11:127–152. doi:10.1016/S1387-2656(05)11004-7
48. Letchuman V, Ampie L, Shah AH, Brown DA, Heiss JD, Chittiboina P. Syngeneic murine glioblastoma models: reactionary immune changes and immunotherapy intervention outcomes. *Neurosurg Focus*. 2022;52(2):E5. doi:10.3171/2021.11.FOCUS21556
49. Martínez-Murillo R, Martínez A. Standardization of an orthotopic mouse brain tumor model following transplantation of CT-2A astrocytoma cells. *Histol Histopathol*. 2007;22(12):1309–1326. doi:10.14670/HH-22.1309
50. Orendorff CJ, Cj M. Quantitation of metal content in the silver-assisted growth of gold nanorods. *J Phys Chem B*. 2006;110(9):3990–3994. doi:10.1021/jp0570972
51. Rinwa P, Eriksson M, Cotgreave I, Bäckberg M. 3R-Refinement principles: elevating rodent well-being and research quality. *Lab Anim Res*. 2024;40(1):11. doi:10.1186/s42826-024-00198-3
52. Fernández-Ruiz R, Redrejo MJ, Friedrich EJ, Ramos M, Fernández T. Evaluation of bioaccumulation kinetics of gold nanorods in vital mammalian organs by means of total reflection X-ray fluorescence spectrometry. *Anal Chem*. 2014;86(15):7383–7390. doi:10.1021/ac5006475
53. Institute for Laboratory Animal Research (U.S.). Committee on Recognition and Alleviation of Distress in Laboratory Animals. *Recognition and Alleviation of Distress in Laboratory Animals*. Washington (DC): National Academies Press (US). 2008. PMID: 20669418.
54. Gupta BD, Dandiya PC, Gupta ML, Gabba AK. An examination of the effect of central nervous system stimulant and anti-depressant drugs on open field performance in rats. *Eur J Pharmacol*. 1971;13(3):341–346. doi:10.1016/0014-2999(71)90224-x
55. Wang Q, Wu H, Hu J, et al. Nestin is required for spindle assembly and cell cycle progression in glioblastoma cells. *Mol Cancer Res*. 2021;19 (10):1651–1665. doi:10.1158/1541-7786.MCR-20-0994
56. Lier J, Streit WJ, Bechmann I. Beyond activation: characterizing microglial functional phenotypes. *Cells*. 2021;10(9):2236. doi:10.3390/cells10092236
57. Hoogland ICM, Houbolt C, van Westerloo DJ, van Gool WA, van de Beek D. Systemic inflammation and microglial activation: systematic review of animal experiments. *J Neuroinflammation*. 2015;12:114. doi:10.1186/s12974-015-0332-6
58. Hussein EA, Zagho MM, Nasrallah GK, Elzatahry AA. Recent advances in functional nanostructures as cancer photothermal therapy. *Int J Nanomed*. 2018;13:2897–2906. doi:10.2147/IJN.S161031
59. Baffou G, Quidant R, Girard C. Heat generation in plasmonic nanostructures: influence of morphology. *Appl Phys Lett*. 2009;94:153109. doi:10.1063/1.3116645
60. Smitha SL, Gopchandran KG, Smijesh N, Philip R. Size-dependent optical properties of Au nanorods. *Prog Nat Sci Mater Int*. 2013;23(1):36–43. doi:10.1016/j.pnsc.2013.01.005
61. Kennedy WJ, Izor S, Anderson BD, Frank G, Varshney V, Ehlert GJ. Thermal Reshaping Dynamics of Gold Nanorods: influence of Size, Shape, and Local Environment. *ACS Appl Mater Interfaces*. 2018;10(50):43865–43873. doi:10.1021/acsami.8b12965
62. Mbalaha ZS, Birch DJS, Chen Y. Photothermal effects of gold nanorods in aqueous solution and gel media: influence of particle size and excitation wavelength. *IET Nanobiotechnol*. 2023;17(2):103–111. doi:10.1049/nbt2.12110
63. Mao W, Son YJ, Yoo HS. Gold nanospheres and nanorods for anti-cancer therapy: comparative studies of fabrication, surface-decoration, and anti-cancer treatments. *Nanoscale*. 2020;12(28):14996–15020. doi:10.1039/d0nr01690j
64. Plan Sangnier A, de Walle A V, Aufaure R, et al. Endosomal Confinement of Gold Nanospheres, Nanorods, and Nanoraspberries Governs Their Photothermal Identity and Is Beneficial for Cancer Cell Therapy. *Adv Biosyst*. 2020;4(4):e1900284. doi:10.1002/adbi.201900284

65. Qin Z, Wang Y, Randrianalisoa J, et al. Quantitative comparison of photothermal heat generation between gold nanospheres and nanorods. *Sci Rep*. 2016;6:29836. doi:10.1038/srep29836
66. Ozcicek I, Aysit N, Cakici C, Aydeger A. The effects of surface functionality and size of gold nanoparticles on neuronal toxicity, apoptosis, ROS production and cellular/suborgan biodistribution. *Mater Sci Eng C*. 2021;128:112308. doi:10.1016/j.msec.2021.112308
67. Bhamidipati M, Fabris L. Multiparametric Assessment of Gold Nanoparticle Cytotoxicity in Cancerous and Healthy Cells: the Role of Size, Shape, and Surface Chemistry. *Bioconjug Chem*. 2017;28(2):449–460. doi:10.1021/acs.bioconjchem.6b00605
68. Paviolo C, Stoddart PR. Gold nanoparticles for modulating neuronal behavior. *Nanomaterials*. 2017;7(4):92. doi:10.3390/nano7040092
69. Yasun E, Li C, Barut I, et al. BSA Modification to Reduce CTAB Induced Nonspecificity and Cytotoxicity of Aptamer-Conjugated Gold Nanorods Graphical Abstract HHS Public Access. *Nanoscale*. 2015;7(22):10240–10248. doi:10.1039/b000000x/HHS
70. Safdar MH, Hussain Z, Abourehab MAS, Hasan H, Afzal S, Thu HE. New developments and clinical transition of hyaluronic acid-based nanotherapeutics for treatment of cancer: reversing multidrug resistance, tumour-specific targetability and improved anticancer efficacy. *Artif Cells Nanomed Biotechnol*. 2018;46(8):1967–1980. doi:10.1080/21691401.2017.1397001
71. Zeng X, Wang H, Zhang Y, Xu X, Yuan X, Li J. pH-Responsive Hyaluronic Acid Nanoparticles for Enhanced Triple Negative Breast Cancer Therapy. *Int J Nanomed*. 2022;17:1437–1457. doi:10.2147/IJN.S360500
72. Edelman R, Assaraf YG, Levitzky I, Shahar T, Livney YD. Hyaluronic Acid-Serum Albumin Conjugate-Based Nanoparticles for Targeted Cancer Therapy. *Oncotarget*. 2017;8(15):24337–24353. doi:10.18632/oncotarget.15363
73. Iorgulescu JB, Ruthen N, Ahn R, et al. Antigen presentation deficiency, mesenchymal differentiation, and resistance to immunotherapy in the murine syngeneic CT2A tumor model. *Front Immunol*. 2023;14:1297932. doi:10.3389/fimmu.2023.1297932
74. Berger G, Knelson EH, Jimenez-Macias JL, et al. STING activation promotes robust immune response and NK cell-mediated tumor regression in glioblastoma models. *Proc Natl Acad Sci U S A*. 2022;119(28):e2111003119. doi:10.1073/pnas.2111003119
75. Khan SM, Desai R, Coxon A, et al. Impact of CD4 T cells on intratumoral CD8 T-cell exhaustion and responsiveness to PD-1 blockade therapy in mouse brain tumors. *J Immunother Cancer*. 2022;10(12):e005293. doi:10.1136/jitc-2022-005293
76. Gudbergsson JM, Christensen E, Kostrikov S, et al. Conventional Treatment of Glioblastoma Reveals Persistent CD44+ Subpopulations. *Mol Neurobiol*. 2020;57(9):3943–3955. doi:10.1007/s12035-020-02004-2
77. Brown DV, Filiz G, Daniel PM, et al. Expression of CD133 and CD44 in glioblastoma stem cells correlates with cell proliferation, phenotype stability and intratumor heterogeneity. *PLoS One*. 2017;12(2):e0172791. doi:10.1371/journal.pone.0172791
78. Yang M, Zhang Y, Hu Z, Xie H, Tian W, Liu Z. Application of hyaluronic acid-based nanoparticles for cancer combination therapy. *Int J Pharm*. 2023;646:123459. doi:10.1016/j.ijpharm.2023.123459
79. Cai J, Fu J, Li R, Zhang F, Ling G, Zhang P. A potential carrier for anti-tumor targeted delivery-hyaluronic acid nanoparticles. *Carbohydr Polym*. 2019;208:356–364. doi:10.1016/j.carbpol.2018.12.074
80. Xu W, Qian J, Hou G, et al. Hyaluronic Acid-Functionalized Gold Nanorods with pH/NIR Dual-Responsive Drug Release for Synergetic Targeted Photothermal Chemotherapy of Breast Cancer. *ACS Appl Mater Interfaces*. 2017;9(42):36533–36547. doi:10.1021/acsami.7b08700
81. Li T, Geng Y, Zhang H, et al. A versatile nanoplatform for synergistic chemo-photothermal therapy and multimodal imaging against breast cancer. *Expert Opin Drug Deliv*. 2020;17(5):725–733. doi:10.1080/17425247.2020.1736033
82. Liu X, Li W, Chen T, et al. Hyaluronic Acid-Modified Micelles Encapsulating Gem-C 12 and HNK for Glioblastoma Multiforme Chemotherapy. *Mol Pharm*. 2018;15(3):1203–1214. doi:10.1021/acs.molpharmaceut.7b01035
83. Li Z, Huang H, Tang S, et al. Small gold nanorods laden macrophages for enhanced tumor coverage in photothermal therapy. *Biomaterials*. 2016;74:144–154. doi:10.1016/j.biomaterials.2015.09.038
84. Licciardi M, Varvarà P, Tranchina L, et al. In vivo efficacy of verteporfin loaded gold nanorods for combined photothermal/photodynamic colon cancer therapy. *Int J Pharm*. 2022;625:122134. doi:10.1016/j.ijpharm.2022.122134
85. Gonçalves DPN, Park DM, Schmidt TL, Werner C. Modular peptide-functionalized gold nanorods for effective glioblastoma multicellular tumor spheroid targeting. *Biomater Sci*. 2018;6(5):1140–1146. doi:10.1039/c7bm01107e
86. Tavianatou AG, Caon I, Franchi M, Piperigkou Z, Galesso D, Karamanos NK. Hyaluronan: molecular size-dependent signaling and biological functions in inflammation and cancer. *FEBS J*. 2019;286(15):2883–2908. doi:10.1111/febs.14777
87. Chistyakov DV, Astakhova AA, Azbukina NV, Goriainov SV, Chistyakov VV, Sergeeva MG. High and low molecular weight hyaluronic acid differentially influences oxylipins synthesis in course of neuroinflammation. *Int J Mol Sci*. 2019;20(16):3894. doi:10.3390/ijms20163894
88. Austin JW, Gilchrist C, Fehlings MG. High molecular weight hyaluronan reduces lipopolysaccharide mediated microglial activation. *J Neurochem*. 2012;122(2):344–355. doi:10.1111/j.1471-4159.2012.07789.x
89. Hayward SL, Wilson CL, Kidambi S. Hyaluronic Acid-Conjugated Liposome Nanoparticles for Targeted Delivery to CD44 Overexpressing Glioblastoma Cells. *Oncotarget*. 2016;7(23):34158–34167. doi:10.18632/oncotarget.8926
90. Riley RS, Day ES. Gold nanoparticle-mediated photothermal therapy: applications and opportunities for multimodal cancer treatment. *Wiley Interdiscip Rev Nanomed Nanobiotechnol*. 2017;9(4):1449. doi:10.1002/wnan.1449
91. Karlsson T, Henriksson R, Hedman H. Induction of Apoptosis in Resistant Glioma Cells by Synthetic Caspase-Activation. *J Neurooncol*. 2004;66 (1–2):71–79. doi:10.1023/b:neon.0000013485.09953.25
92. Cabada TF, de Pablo CSL, Serrano AM, Guerrero FP, Olmedo JJS, Gomez MR. Induction of cell death in a glioblastoma line by hyperthermic therapy based on gold nanorods. *Int J Nanomed*. 2012;7:1511–1523. doi:10.2147/IJN.S28470
93. Michalczyk M, Humeniuk E, Adamczuk G, Korga-Plewko A. Hyaluronic Acid as a Modern Approach in Anticancer Therapy-Review. *Int J Mol Sci*. 2022;24(1):103. doi:10.3390/ijms24010103
94. Xu W, Qian J, Hou G, et al. A dual-targeted hyaluronic acid-gold nanorod platform with triple-stimuli responsiveness for photodynamic/photothermal therapy of breast cancer. *Acta Biomater*. 2019;83:400–413. doi:10.1016/j.actbio.2018.11.026
95. Gao D, Wong RCH, Wang Y, Guo X, Yang Z, Lo PC. Shifting the absorption to the near-infrared region and inducing a strong photothermal effect by encapsulating zinc(II) phthalocyanine in poly(lactic-co-glycolic acid)-hyaluronic acid nanoparticles. *Acta Biomater*. 2020;116:329–343. doi:10.1016/j.actbio.2020.08.042